

Application of Transient Evanescent Grating Techniques to the Study of Liquid/Liquid Interfaces

Pierre Brodard[†] and Eric Vauthey*

Department of Physical Chemistry, University of Geneva, 30 Quai Ernest-Ansermet, CH-1211 Geneva, Switzerland

Received: October 26, 2004; In Final Form: December 21, 2004

Transient grating experiments performed with evanescent fields resulting from total internal reflection at an interface between a polar absorbing solution and an apolar transparent solvent are described. The time evolution of the diffracted intensity was monitored from picosecond to millisecond time scales. The diffracted signal originates essentially from two density phase gratings: one in the absorbing phase induced by thermal expansion and one in the transparent solvent due to electrostriction. A few nanoseconds after excitation, the latter grating is replaced by a thermal grating due to thermal diffusion from the absorbing phase. The speed of sound and the acoustic attenuation measured near the interface are found to be essentially the same as in the bulk solutions. However, after addition of a surfactant in the polar phase, the speed of sound near the interface differs substantially from that in the bulk with the same surfactant concentration. This effect is interpreted in terms of adsorption at the liquid/liquid interface. Other phenomena, which are not observed in bulk experiments, such as acoustic echoes and a fast oscillation of the signal intensity, are also described.

Introduction

Liquid/liquid interfaces play a major role in various areas of sciences and technology.¹ For example, they act as a catalyst for chemical extraction processes. In biology, oil/water interfaces can be considered as simple models of cell membranes. Moreover, in pharmaceutical sciences, the kinetics of chemicals delivery through lipid bilayers is a key factor for the efficiency of any drug.

Spectroscopic information on the interfaces is not easily accessible because, in most cases, the signal arising from this region is totally buried in that originating from the bulk. To circumvent this problem, two approaches have been proposed. The first is to probe a property specific to interfaces, like for example the second order nonlinear susceptibility, which essentially vanishes in centrosymmetric material.² The vibrational sum frequency spectroscopy has been shown to yield a rather precise structural picture of molecules at liquid interfaces.³ Surface second harmonic generation is another variant of this technique, which can be used to probe dynamics at the interface.^{4,5} Finally, the transient reflecting grating technique is a four-wave mixing method that probes the photoinduced changes of reflectivity of the interface.^{6,7} The main drawback of all these techniques is the impossibility to have a control of the thickness of the probed region. Consequently, the depth profile of a given property cannot be investigated.

The second approach consists of confining the optical beams within a small volume close to the interface. For example, the application of near-field Raman spectroscopy for probing liquid/liquid interfaces has recently been demonstrated.⁸ Although this technique can be carried out at different distances from the interface, it does not yield information on the dynamics of the

system. Confinement can also be obtained by using evanescent optical fields, generated by total internal reflection (TIR). In TIR fluorescence, an evanescent wave excites the sample,^{9,10} while in attenuated TIR, the evanescent wave is involved in the probing process.¹¹ Information on the interfacial dynamics can be obtained by both TIR fluorescence and attenuated TIR; however, the first technique is limited to fluorescent probes, while the second suffers from a relatively poor sensitivity.¹¹

Transient grating (TG) techniques are known to combine the advantage of the fluorescence spectroscopy, namely its high sensitivity due to the zero-background nature of the signal, with that of transient absorption, because of its sensitivity to absorption changes.^{12–15} A further advantage of the TG techniques is their sensitivity to photoinduced changes of refractive index. Because of this, various thermoacoustic properties of a material can be investigated.^{16,17} TG with evanescent waves has already been discussed theoretically.¹⁸ Its application to investigate solid/liquid interfaces has already been demonstrated.^{19,20} Recently, we have briefly reported on the implementation of this technique to liquid/liquid interfaces.²¹

We report here on a TG investigation of the thermoacoustic properties of binary liquid systems performed with evanescent waves generated upon TIR at the liquid/liquid interface. It will be shown that the nature of the TG signal is more complex than assumed originally.²¹ The observation of several phenomena such as acoustic echoes is also reported. Finally, we show that these techniques can be used for monitoring the adsorption of a surfactant at a liquid/liquid interface.

Principle of the Techniques

Transient Density Phase Grating. The principle of the TG techniques has been described in detail in several papers.^{12–16} We will briefly review here the most important features. In a conventional TG experiment, the sample is excited by two crossed and time coincident laser pump pulses. Resonant and

[†] Present address: Department of Chemistry, Graduate School of Science, Tohoku University, Sendai 980-8578, Japan.

* Address correspondence to this author. E-mail: eric.vauthey@chiphys.unige.ch

nonresonant optical interactions between the sample and the spatially modulated light lead to a spatial modulation of the refractive index, n , a so-called phase grating, and of the absorbance, A , an amplitude grating. The magnitude of the grating vector, q_g , is given by

$$q_g = \frac{2\pi}{\Lambda} \quad \text{with} \quad \Lambda = \frac{\lambda_{pu}}{2 \sin(\theta_{pu}/2)} \quad (1)$$

where Λ is the fringe spacing, λ_{pu} the pump wavelength, and θ_{pu} the crossing angle of the pump pulses.

A third laser pulse, striking these gratings at the Bragg angle, θ_B , is partially diffracted. In the case of weak modulation, the ratio of the diffracted and probe light intensities, I_{dif}/I_{pr} , depends on the square of the modulation amplitudes of the absorbance and refractive index, ΔA and Δn , respectively:

$$\frac{I_{dif}}{I_{pr}} \cong \left[\left(\frac{\ln(10) \cdot \Delta A}{4 \cos \theta_B} \right)^2 + \left(\frac{\pi d \Delta n}{\lambda_{pr} \cos \theta_B} \right)^2 \right] \exp \left(-\frac{\ln(10) \cdot A}{\cos \theta_B} \right) \quad (2)$$

where d is the grating thickness and λ_{pr} the probe wavelength. The exponential term reflects the absorption of the diffracted signal by the sample. Whereas the modulation of absorbance is essentially related to the modulation of population, the variation of refractive index can have several origins:

$$\Delta n = \Delta n_p + \Delta n_d + \Delta n_{OKE} \quad (3)$$

where Δn_p is due to population changes and is Kramers-Kronig related to ΔA , Δn_d arises from density changes, and Δn_{OKE} is related to the optical Kerr effect. The latter effect is nonresonant and is only significant when working with intense optical pulses. This term will thus be neglected further on.

In the experiments presented here, the excited state population of the absorber decays nonradiatively within a few tens of picoseconds. Once this decay is over, eq 2 reduces to

$$\frac{I_{dif}}{I_{pr}} = \left(\frac{\pi d}{\lambda_{pr} \cos \theta_B} \right)^2 \cdot \Delta n_d^2 \quad (4)$$

The modulation amplitude of the density phase grating can be due to electrostriction (ES), thermal expansion (TE), and volume changes (VC):

$$\Delta n_d = \Delta n_d^{ES} + \Delta n_d^{TE} + \Delta n_d^{VC} \quad (5)$$

Volume changes are only significant if the molecular volume and its environment vary markedly upon excitation. This contribution can be neglected here, because the excited-state population is very short lived.

Electrostriction is a nonresonant interaction that leads to material compression in the region of high electric field strength. The periodic compression is accompanied by the generation of two counter-propagating acoustic waves with wave vectors, $\vec{q}_{ac} = \vec{q}_g = \pm(2\pi/\Lambda)\vec{t}$, where \vec{t} is the unit vector along the modulation axis. The interference of these acoustic waves leads to a temporal modulation of Δn_d^{ES} at the acoustic frequency f_{ac} .¹⁷

$$\Delta n_d^{ES}(t) = -C^{ES} \sin(2\pi f_{ac} t) \exp(-\alpha v_{ac} t) \quad (6)$$

with

$$2\pi f_{ac} = q_{ac} v_{ac} \quad (7)$$

where C^{ES} is a constant that depends on material properties,

such as the optoelastic constant of the sample, α the acoustic attenuation constant, and v_{ac} the speed of sound. As Δn_d^{ES} oscillates between negative and positive values, the diffracted intensity, which is proportional to $(\Delta n_d^{ES})^2$, shows a temporal oscillation at twice the acoustic frequency. In most cases, Δn_d^{ES} is weak and can be neglected if the pump pulses are within an absorption band of the sample.

Thermal expansion is often the dominant term when pumping resonantly. Indeed, in most cases, part of the optical excitation energy is released as heat through nonradiative transitions. In the case of prompt heat release, thermal expansion is impulsive and is, like electrostriction, accompanied by the generation of two counter-propagating acoustic waves with the same wave vectors, \vec{q}_{ac} . As this standing acoustic wave oscillates, it interferes with the thermal diffusive grating, and as a consequence, the time dependence of Δn_d^{TE} differs from that of eq 6:

$$\Delta n_d^{TE}(t) = C^{TE} [1 - \cos(2\pi f_{ac} t) \exp(-\alpha v_{ac} t)] \exp(-D_{th} q_g^2 t) \quad (8)$$

with

$$C^{TE} = \left(\frac{\beta}{\rho C_p} Q \right) \rho \frac{\partial n}{\partial \rho} \quad (9)$$

where D_{th} is the thermal diffusivity constant, β the cubic thermal expansion constant, ρ the density, C_p the heat capacity at constant pressure, and Q the amount of heat deposited per unit volume.

The time profile of the diffracted intensity originating from Δn_d^{TE} exhibits first an oscillation at the frequency f_{ac} , which is damped because of acoustic attenuation. The ensuing diffracted intensity decays to zero as a consequence of thermal diffusion.

If the magnitude of the grating vector, q_g , is known, the speed of the sound, the acoustic attenuation constant, and the thermal diffusivity constant can be easily extracted from the time profile of the diffracted intensity. If the excited population is longer lived, interference between population and density phase gratings can lead to a rather complex time profile of the diffracted intensity,^{22,23} and make the determination of the above-mentioned properties much more difficult.

The bulk modulus, B , can then be calculated from the speed of sound and the density ρ :

$$B = v_{ac}^2 \rho \quad (10)$$

Similarly, the thermal conductivity, λ_{th} , can be deduced from the thermal diffusivity:

$$\lambda_{th} = D_{th} \rho C_p \quad (11)$$

Evanescent Waves. An optical beam with a wavelength, λ , propagating in a medium with a refractive index, n_h , and striking an interface with a medium having lower refractive index, n_l , at an angle of incidence, θ_i , larger than the critical angle, $\theta_c = \arcsin(n_l/n_h)$, undergoes TIR. In this case, a bound electromagnetic field, the evanescent wave, is present in the low refractive

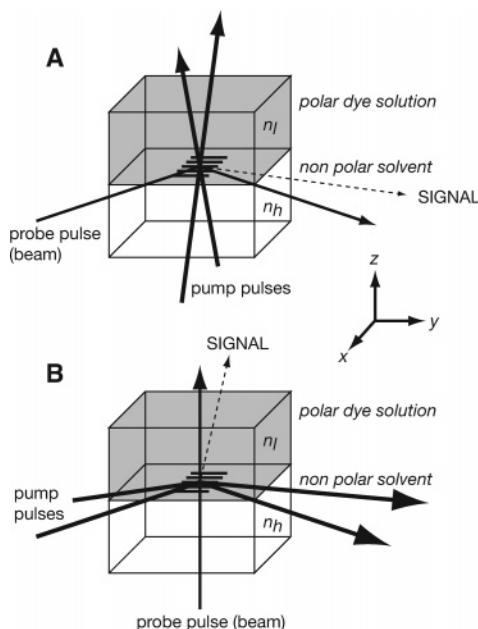


Figure 1. Transient evanescent grating geometries: (A) TIR-probe and (B) TIR-pump.

index medium. Its corresponding intensity, I , decays exponentially as a function of the distance, z , from the interface:

$$I(z) = I_0 \exp(-z/d_p) \quad (12)$$

where I_0 is the intensity at $z = 0$, and d_p is the penetration depth:

$$d_p = \frac{\lambda}{4\pi\sqrt{n_h^2 \sin^2 \theta_i - n_l^2}} \quad (13)$$

Transient Evanescent Grating (TEG). In the experiments presented here, the transient density phase grating technique is performed with evanescent fields. Three different optical beam geometries can be envisaged: TIR-probe,²⁰ TIR-pump,^{18,19} and all-TIR. In the TIR-probe mode (Figure 1A), the two pump pulses are crossed perpendicularly to the interface, generating a thick grating near the contact surface. The evanescent probe field interacts with a 70 to 120 nm thick layer of this grating, depending on the angle of incidence, and the diffracted signal reemerges in the high refractive index medium.

In the TIR-pump geometry (Figure 1B), the spatially modulated optical field at the interface penetrates the low refractive medium as an evanescent wave. Upon resonant interaction with the low refractive medium, density and/or amplitude evanescent gratings are generated. These are thin gratings and therefore the Bragg condition is no longer required for probing. Because the diffracted intensity depends on the square of the pump pulse intensity, the penetration depth is smaller by a factor of 2 than in the TIR-probe geometry. In this case, the probe pulse has to cross the whole absorbing solution and therefore probing has to be performed at a different wavelength than pumping.

The best spatial resolution, about 30 nm, is achieved with the all-TIR geometry. However, this geometry is experimentally more delicate and therefore has not been used very intensively here.

Experimental Details

Optical Setups. Two different TG setups have been used, depending on the time window investigated. In both cases, excitation was achieved by the frequency doubled output pulses

at 532 nm of an active–passive mode-locked and cavity dumped Nd:YAG laser (Continuum PY61-10). Pumping was achieved by splitting about 60% of this output into two pulses, which were then crossed at the sample. The beam diameter at the sample was around 2 mm and the energy was typically of the order of 1 mJ.

For measurement in the 0–4 ns time window, pump-probe detection was used.²⁴ The remaining 40% of the laser output was sent along an optical delay line before being focused onto the grating. For bulk experiments, the three pulses were arranged in a boxcars geometry. For interfacial experiments, the TIR beams passed through a cylindrical lens ($f = 500$ mm) in order to achieve circular spots on the interface. With the crossing angle used ($30^\circ < \theta_{pu} < 60^\circ$), the acoustic frequency, f_{ac} , was of the order of 1–2 GHz. The diffracted signal was detected with a vacuum photodiode, whose output was amplified before being sent into a computer.

Real time detection was used for measurements in longer time scales.²⁵ Probing was achieved at 781 nm with a 0.5 W multimode cw laser diode (Semiconductor Laser International Corporation). The diffracted signal was detected with a photomultiplier tube (Hamamatsu R928) connected to a 500 MHz digital oscilloscope (Tektronix TDS 620A). To resolve the propagation of the acoustic waves with this setup, their frequency was set to about 50–100 MHz, by crossing the pump pulses at an angle varying between 1° and 3° .

Samples. The absorbers, malachite green (MG), rhodamine 6G (R6G, Acros), and rhodamine 110 (R110, Acros), the solvents, acetonitrile (ACN), carbon disulfide (CS_2), decalin (DEC, cis/trans mixture), dodecane (DOD), methanol (MeOH), ethanol (EtOH), and propionitrile (PrCN), and the surfactant, sodium dodecyl sulfate (SDS), were of the highest commercially available purity and were used without further purification. Water was distilled twice and *N,N*-dimethylaniline (DMA, Acros) was distilled under inert atmosphere. If not specified, all compounds were from Fluka.

For bulk measurements, the sample solutions were poured in a 1 mm thick quartz cell and were stirred by N_2 -bubbling. The absorbance of the samples at 532 nm amounted to about 0.2 over 1 mm.

For TIR measurements, a $4 \times 4 \times 4$ cm³ cell with five optical glass windows was used. For DEC/water and DOD/water systems, about 5 mL of the aqueous dye solutions was first poured in the cell. About 20 mL of the less dense DEC or DOD was then added on top. On the other hand, the ACN, MeOH, and PrCN dye solutions were located above the apolar phase. No significant sample degradation could be observed after the measurements.

Results and Discussion

Measurements in Bulk Solutions. To check the reliability and precision of the various optical setups, some measurements have first been performed in bulk solutions. Figure 2 shows the time profile of the diffracted intensity measured with the pump-probe setup after excitation of MG in MeOH. The crossing angle was 42° corresponding to a fringe spacing of $0.75 \mu\text{m}$. The spike at time zero is the contribution of the population to the signal, the ground-state recovery of MG in MeOH occurring nonradiatively within a few picoseconds.²⁶ The periodic oscillations are due to the resulting impulsive thermal expansion. The black line is the best fit of eqs 4 and 8, with $q_g = q_{ac}$ and $D_{th} = 0$ as fixed parameters and C^{TE} , α , and v_{ac} as adjustable parameters.

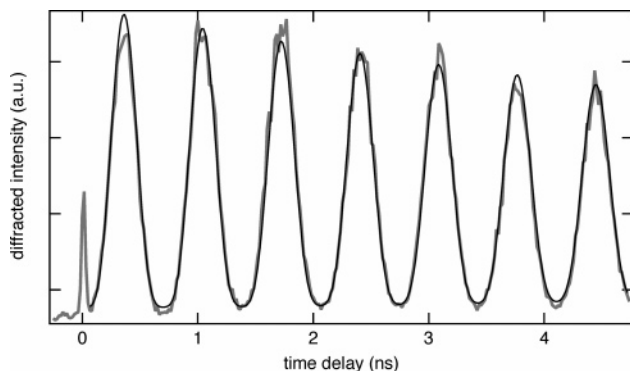


Figure 2. Time profile of the diffracted intensity measured with a solution of MG in MeOH using the pump-probe setup. The black line is the best fit of eqs 4 and 8.

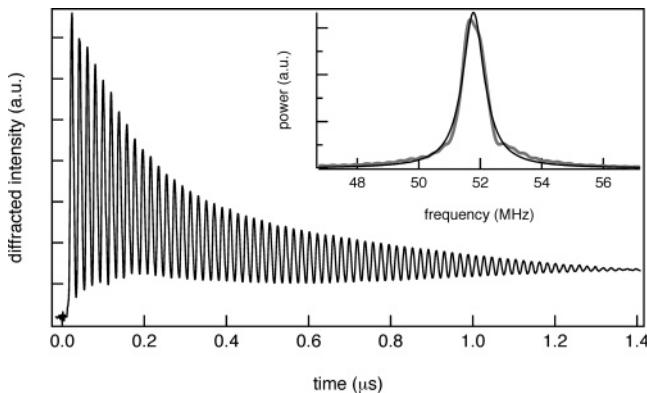


Figure 3. Time profile of the diffracted intensity measured with a solution of MG in MeOH with the cw-probe setup. Inset: Power spectrum obtained upon Fourier transformation of the time profile.

On the other hand, Figure 3 shows the time profile of the diffracted intensity measured with the same sample but with the cw-probe setup. Because of the limited response time of this setup, θ_{pu} was strongly reduced in order to achieve a smaller acoustic frequency.

The acoustic frequency was not determined from the fit of eqs 4 and 8 but rather from the power spectrum obtained by fast Fourier transformation of the time profile. This spectrum is shown in the inset of Figure 3 together with the best fit of a Lorentzian line shape. This procedure yields a precise acoustic frequency and thus a reliable speed of sound can be obtained, provided the magnitude of the grating vector is known accurately (see eq 7).

In principle, the acoustic attenuation constant can be determined from the full width at half-maximum of the power spectral line. However, because of the limited response time of the cw-probe setup, the time profile is somewhat distorted and therefore a reliable value of α cannot be readily obtained. Nevertheless, this drawback can in principle be overcome by using a faster detector or by deconvolving the instrument response function from the measured time profile.

Similar time profiles have been obtained using R6G instead of MG. However, to enhance the nonradiative deactivation of the excited R6G molecules, a small amount of DMA has been added to the solution. This results in a substantial shortening of the S_1 lifetime of R6G, because of the occurrence of electron-transfer quenching.²⁷

Figure 4 shows the time profile of the diffracted intensity measured with the pump-probe setup in pure DEC. The fringe spacing was 0.94 μm corresponding to an acoustic frequency of 1.46 GHz. As there is no absorber in the sample, the origin

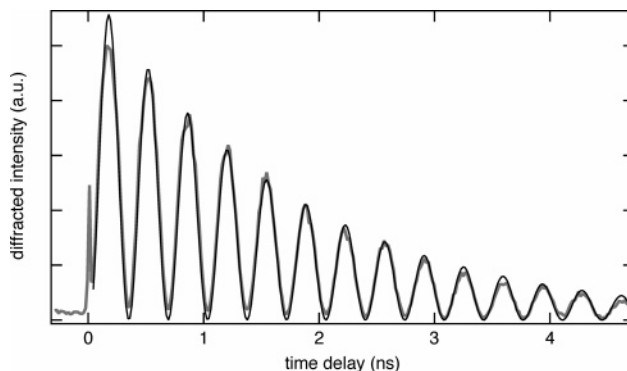


Figure 4. Time profile of the diffracted intensity measured with pure DEC using the pump-probe setup. The black line is the best fit of eqs 4 and 6.

TABLE 1: Speed of Sound, v_{ac} , Acoustic Attenuation Constant, α/f_{ac}^2 , and Bulk Modulus, B , in Various Solvents Measured by Transient Grating and Literature Values

| solvent | v_{ac} ($\text{m}\cdot\text{s}^{-1}$) | | $\alpha/f_{ac}^2 \times 10^{15}$ ($\text{s}^2\cdot\text{m}^{-1}$) | | $B \times 10^{-8}$ ($\text{N}\cdot\text{m}^{-2}$) | |
|------------------|---|-------------------|---|-------------------|---|--------------------|
| | measd | lit. | measd | lit. | measd | lit. |
| MeOH | 1117 | 1121 ^a | 31.3 | 30.2 ^d | 9.88 | 8.24 ^a |
| EtOH | 1159 | 1162 ^a | 49.9 | 55.0 ^d | 10.59 | 8.94 ^a |
| ACN | 1305 | 1303 ^b | 82.4 | | 13.37 | |
| PrCN | 1291 | 1264 ^c | | | 13.03 | 12.32 ^c |
| H ₂ O | 1496 | 1497 ^a | | | 22.34 | 21.78 ^a |
| DEC | 1370 | 1403 ^b | 101.8 | | 16.83 | |
| CS ₂ | 1122 | 1140 ^a | | | 15.90 | |

^a From ref 28. ^b From ref 29. ^c From ref 30. ^d From ref 17.

of the signal is purely nonresonant. The initial spike is due to the optical Kerr effect, while the oscillating signal originates from electrostriction. The continuous line is the best fit of eqs 4 and 6 to the data after the end of the Kerr response. Contrary to the signal arising only from thermal expansion, the diffracted intensity due to electrostriction vanishes exactly twice during an acoustic period, $\tau_{ac} = f_{ac}^{-1}$, which amounts to 685 ps in this measurement, and intensity maxima occur at $(2n + 1)\tau_{ac}/4$, $n = 0, 1, 2, \dots$

These measurements have been repeated in several solvents. The speed of sound, v_{ac} , the acoustic attenuation constant, α , obtained from their analysis, and the bulk modulus, B , calculated with eq 10 are listed in Table 1. As the speed of sound is independent of the frequency, the values obtained with both the pump-probe and the cw-probe techniques can be readily compared. However, the standard deviation on the measured speeds is much smaller with the cw-probe setup. This is not surprising as the number of oscillations recorded is much larger in this case.

Because of the aforementioned problem with the cw-probe setup, the acoustic attenuation constant has been extracted from the pump-probe data only. As α is proportional to the square of the acoustic frequency, α/f_{ac}^2 values are listed.

Both v_{ac} and α were found to be independent of the absorber, MG or R6G+DMA, as long as the concentration of DMA used to quench the excited state of R6G was kept low ($[\text{DMA}] < 0.02 \text{ M}$). In MeOH, larger DMA concentrations resulted in an increase of the speed of sound. For example, $v_{ac} = 1137$ and 1164 ms^{-1} with 0.02 and 0.1 M DMA, respectively. On the other hand, the effect of large DMA concentrations on α was not investigated.

As shown in Table 1, the measured v_{ac} values are in excellent agreement with those reported in the literature, while the α/f_{ac}^2 values compare rather well. These results confirm the reliability

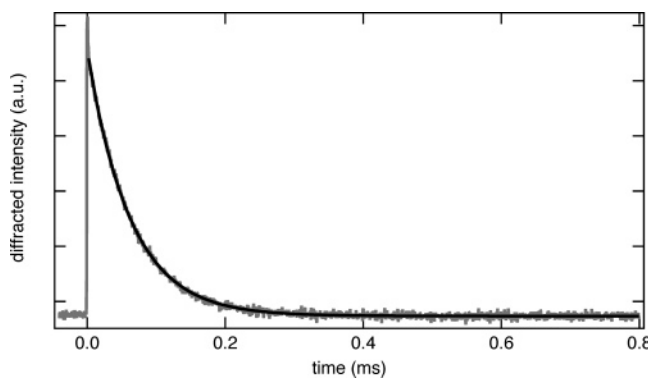


Figure 5. Decay of the diffracted intensity measured with a solution of MG in MeOH using the cw-probe setup. The black line is the best exponential fit.

TABLE 2: Thermal Diffusivity, D_{th} , and Thermal Conductivity, λ_{th} , in Various Solvents Measured by Transient Grating and Literature Values

| solvent | $D_{th} \times 10^8$ ($\text{m}^2 \cdot \text{s}^{-1}$) | | λ_{th} ($\text{W} \cdot \text{m}^{-1} \cdot \text{s}^{-1}$) | |
|------------------|---|-------------------|---|--------------------|
| | measd | lit. | measd | lit. |
| MeOH | 9.9 | 10.0 ^a | 0.199 | 0.200 ^c |
| EtOH | 9.3 | 8.8 ^a | 0.179 | 0.169 ^c |
| ACN | 10.3 | 10.8 ^a | 0.180 | 0.188 ^c |
| PrCN | 9.6 | | 0.163 | |
| H ₂ O | 14.6 | 14.5 ^b | 0.609 | 0.607 ^c |

^a From ref 31. ^b From ref 32. ^c From ref 28.

of both TG setups and are a further confirmation of the ability of the TG technique for determining the acoustic properties of materials.¹⁷

Figure 5 shows the decay of the diffracted intensity measured with a solution of MG in MeOH using the cw-probe setup. Apart from the first few microseconds, the decay can be well reproduced with an exponential function. The resulting decay time, τ_{obs} , is related to the thermal diffusivity constant as:

$$\tau_{obs} = (2D_{th}q_g^2)^{-1} = \frac{\Lambda^2}{8\pi^2 D_{th}} \quad (14)$$

The D_{th} values measured in various solvents and the resulting thermal conductivities, λ_{th} , calculated with eq 11 are listed in Table 2 together with literature values. In this case again, a very good agreement between both sets of data is obtained, confirming the appropriateness of this method for the determination of diffusion constants.³³

Measurements at Interfaces. With the TEG techniques, acoustic waves can now be generated and monitored in the interfacial region. Acoustic waves at solid interfaces have been intensively studied, and for instance elastic waves are known to be guided by free solid surfaces.³⁴ Such surface acoustic waves (SAWs), where most of the energy remains near the surface, their penetration depth being of the order of one wavelength, are called Rayleigh waves. They travel along the surface of solids with a slightly lower velocity (5–13%) than shear waves, the slowest acoustic waves in bulk solids. At solid/liquid interfaces, Rayleigh waves are still present if they are faster than the liquid bulk waves. However, since a small fraction of their energy dissipates into the liquid, they are called leaky-Rayleigh waves. Scholte–Stoneley or Gogoladze waves are other acoustic waves that are confined at solid/liquid interfaces.³⁵ Their energy decays exponentially into both the solid and the liquid phases, and for a large acoustic impedance mismatch, their velocity is just below the bulk velocity in the

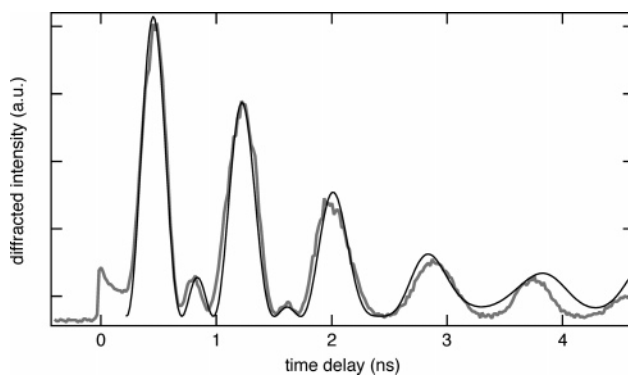


Figure 6. Time profile of the diffracted intensity measured with a solution of R6G in MeOH in contact with DEC using the pump-probe setup and the TIR-probe geometry ($d_p = 83$ nm). The black line is the best fit of eqs 4, 6, and 8.

liquid. For example, the velocity of leaky-Rayleigh waves at the TiO₂/H₂O interface had been measured to be close to that of pure Rayleigh waves, while Scholte–Stoneley waves were found to propagate at a slightly slower speed (1–2%) than bulk wave in water.^{36,37} While several studies on capillary waves have been reported,^{38–41} essentially nothing is known on acoustic waves at liquid/liquid interfaces.

Speed of Sound. Figure 6 presents the first 5 ns of the time profile of the diffracted intensity measured with a MeOH solution of R6G in contact with DEC. This measurement has been performed with the pump-probe setup using the TIR-probe geometry. The penetration depth of the evanescent probe beam was 83 nm. At the relatively high concentration required for such measurements, $> 5 \times 10^{-3}$ M, R6G forms aggregates, which shorten the S₁ lifetime of the monomer by energy transfer quenching.⁴² The ensuing excited aggregates decay nonradiatively with a time constant of the order of 1 ps. Therefore, these measurements do not require the addition of DMA to accelerate the nonradiative relaxation of the R6G excited state. The initial diffracted intensity peak in Figure 6 is essentially due to the contribution of population changes. After this spike, the diffracted intensity exhibits a complex oscillation. Contrary to the profiles measured in the bulk (see Figures 2–4), the period between two intensity peaks is not constant. This behavior can be explained in terms of the interference between two acoustic waves with slightly different frequencies. The presence of small intensity maxima at about 0.8 and 1.6 ns indicate a probable contribution of electrostriction to the signal. The continuous line is the best fit of eq 4 with $\Delta n_d(t)$ given by the sum of eqs 6 and 8. A reasonable agreement with the measured profile is obtained when assuming the propagation of an acoustic wave generated by thermal expansion at 1.16 GHz and of a second acoustic wave at 1.36 GHz induced by electrostriction. From this frequency, the speed of the latter acoustic wave amounts to 1370 m/s, a value that is identical with the speed of sound in pure DEC (see Table 1).

Therefore, in the TIR-probe geometry (see Figure 1A), the probe beam sees first a density phase grating generated by electrostriction in the transparent apolar phase. The evanescent probe field interacts with a grating, essentially a density phase grating, generated by the nonradiative deactivation of excited R6G in MeOH. In principle, the contribution of electrostriction is much weaker than that of thermal expansion.¹⁷ However, with both TIR-probe and TIR-pump geometries, the interaction length of the probe field with the ES grating is much longer than that with the TE grating. Because of the different speeds of sound in these two liquid phases, the frequencies of the acoustic waves

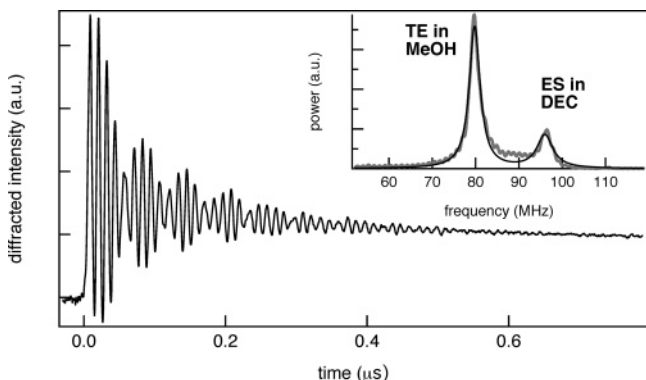


Figure 7. Time profile of the diffracted intensity measured with a solution of R6G in MeOH in contact with DEC using the cw-probe setup and the TIR-pump geometry ($d_p = 40$ nm). Inset: Power spectrum obtained upon Fourier transformation of the time profile.

differ, and therefore a beating pattern can be observed in the time profile of the diffracted intensity. The time window of the pump-probe experiment is, however, too narrow to observe such a beating. Because of this, the presence of a second acoustic wave at a different frequency is not clear. For this reason, in a preliminary report, the ES contribution was thought to originate from the alcoholic phase only.²¹ Actually, no signal can be detected with pure bulk MeOH, while the electrostrictive response in pure bulk DEC is strong, as shown in Figure 4. Because of this misinterpretation, the values of the speed of sound at the interface listed in this preliminary report²¹ should be discarded.

Figure 7 illustrates the time profile of the signal intensity measured with the same sample but using the cw-probe setup and TIR pumping with a penetration depth of 40 nm. For this measurement, the fringe spacing was increased to about 14 μm , resulting in acoustic frequencies of 80 MHz for TE in MeOH and 96 MHz for ES in DEC. The beating pattern due to the interference of the two acoustic modulations is now very clear. The power spectrum obtained by Fourier transform of the time profile (Figure 7 inset) exhibits two distinct peaks that can be reproduced by Lorentzian line shapes.

As electrostriction in DEC is essentially a bulk process, the speed of sound in this experiment should be the same as that in pure DEC, in agreement with the analysis of the pump-probe data. Therefore, the grating vector can be determined very precisely from the acoustic frequency of the ES contribution using eq 7. This is particularly useful as an accurate determination of q_g from the very small crossing angles used in the cw-probing setup is difficult.

While the ES contribution is very useful for internal calibration, it also acts as a local oscillator that enhances the interfacial TE signal. Actually, due to the nanometer size volume in which thermal expansion takes place, the intrinsic TEG signal might even not be detectable without this heterodyning by the ES signal.

While the oscillation at the double acoustic frequency originating from electrostriction is clearly visible in the pump-probe data (see Figure 6), it cannot be distinguished in the time profiles recorded with the cw-probe setup. One can therefore wonder if the 96 MHz acoustic wave observed in this time profile is due to electrostriction only. Indeed, a faint fluorescence that arises from R6G can be observed in the DEC phase upon 532 nm excitation. Therefore a thermal density grating due to the nonradiative deactivation of R6G in the S_1 state might be present in the DEC phase as well. The time constant associated with the heat release from R6G upon deactivation from the S_1

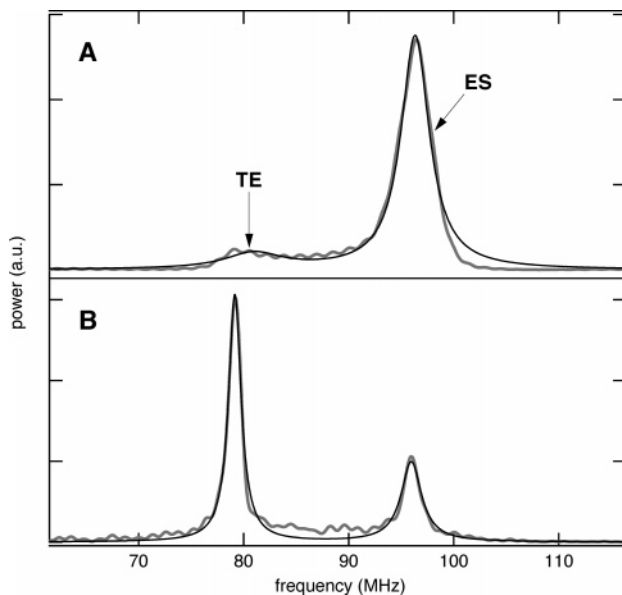


Figure 8. Power spectra of the time profiles of the signal intensity measured with R6G in MeOH in contact with DEC using (A) the TIR-probe geometry ($d_p = 116$ nm) and (B) the TIR-pump geometry ($d_p = 43$ nm). The black lines are the best fits of Lorentzian functions.

state is of the order of 4 ns.⁴³ The shape of the time profile due to such a 4 ns heat release depends on the fringe spacing and more precisely on the acoustic period, τ_{ac} .¹⁶ If $\tau_{ac} \gg 4$ ns, the time profile is totally modulated at the acoustic frequency and is similar to that shown in Figure 2. On the other hand, if $\tau_{ac} \ll 4$ ns, the time profile of the diffracted intensity exhibits a smooth rise that directly reflects the heat release dynamics. In the pump-probe setup, the acoustic period is shorter than 1 ns, and therefore the oscillations observed in the time profile are not due to thermal expansion in DEC. On the other hand, the acoustic period in the cw-probe setup is typically of the order of 10 ns and, in this case, a 4 ns heat release gives rise to a modulated signal.

However, if such a thermal grating is formed in DEC, it must not contribute significantly to the time profile measured with the cw-probe setup for two reasons. First, the concentration of R6G in DEC is very small ($[R6G] < 5 \times 10^{-8}$ M) and the fluorescence quantum yield of R6G at low concentrations is large, namely $\Phi_{fl} = 0.94$.⁴⁴ Therefore, the amount of energy released as heat in DEC is insignificant. Second, the fact that no oscillation at the double acoustic frequency is observed in Figure 7 can be accounted for by the limited time resolution of the setup. Indeed, this time profile and the corresponding Fourier transform can be qualitatively well reproduced by convolving the instrument response function with the diffracted intensity calculated using eqs 6 and 8, assuming that Δn_d^{ES} and Δn_d^{TE} are only present in DEC and MeOH, respectively. The addition of a contribution of Δn_d^{TE} in DEC to the signal leads to a deterioration of the agreement between the simulated and observed profiles.

Interestingly, the relative magnitude of the ES and TE contributions to the signal depends on the experimental geometry. As shown in Figure 8, the contribution of thermal expansion dominates the signal in the TIR-pump geometry, whereas in both the TIR-probe and all-TIR geometries, the signal arises mostly from the nonabsorbing phase. This can be understood by considering that in the TIR-pump geometry the interaction length of the probe beam with the ES grating is substantially smaller than that in the other two arrangements.

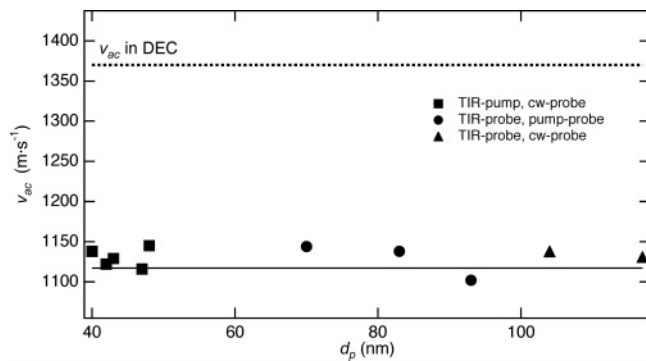


Figure 9. Penetration depth dependence of the speed of sound for the system R6G in MeOH in contact with DEC. The black line is the literature value of the speed of sound in bulk MeOH.²⁸

Similarly, for any geometry, the contribution of thermal expansion to the signal increases with increasing penetration depth. This is a reasonable result, as a large penetration depth implies a thicker TE evanescent grating in the TIR-pump geometry or a longer interaction length with the TE grating in the TIR-probe configuration.

Finally, the relative contribution of both mechanisms to the signal was found to depend on the angle of incidence of the probe beam onto the grating, θ_{pr} . The contribution of electrostriction is the largest in the phase-matching condition, namely with $\theta_{pr} = \theta_B$. Deviation from θ_B results in a net decrease of the ES contribution while keeping the signal intensity due to TE essentially unchanged. This is due to the thick-grating nature of the ES grating, which requires the Bragg condition for efficient diffraction. In the TIR-pump geometry, the TE grating is an evanescent grating and is thus intrinsically thin, i.e., $\Lambda \gg d$. In the TIR-probe geometry, the evanescent probe beam interacts only with a thin layer of the TE grating and thus “sees” a thin grating.

As seen before, the acoustic frequency related to electrostriction in DEC allows a precise determination of the grating vector, which is itself required for obtaining the speed of sound in the polar phase. This latter value was found to be essentially the same as that measured in the bulk solutions. No significant difference could be observed in MeOH, ACN, PrCN, and H₂O in contact with DEC. As illustrated in Figure 9, the speed of sound is independent of the penetration depth. The relatively large scattering of the v_{ac} values shown in this figure can be explained by the different experimental arrangements used for the measurements. Moreover, the speed of sound does not depend on the absorbing dye (R6G or R110) and is not influenced by the nature of the adjacent high refractive index solvent (DEC or DOD).

Only a rough estimate of the acoustic attenuation constant near the interface could be obtained. This is due to the limited time window of the pump-probe experiment and to the interference between the ES and TE contributions. Consequently, the error on α near the interface is too large to be able to establish a difference with the bulk value.

Thermal Diffusion. As in the bulk phase, the slow decay of the diffracted intensity measured near the interface can be well reproduced with an exponential function. However, the value of the thermal diffusivity, D_{th} , calculated according to eq 14 differs from that measured in the bulk. Figure 10 and Table 3 show that the thermal diffusivity at the DEC/MeOH interface exhibits a significant dependence on the penetration depth, d_p . Indeed, the measured D_{th} increases continuously from 7.7×10^{-8} to $9.2 \times 10^{-8} \text{ m}^2 \text{ s}^{-1}$ by going from a penetration depth of 33 to 117 nm. This dependence can be reasonably well

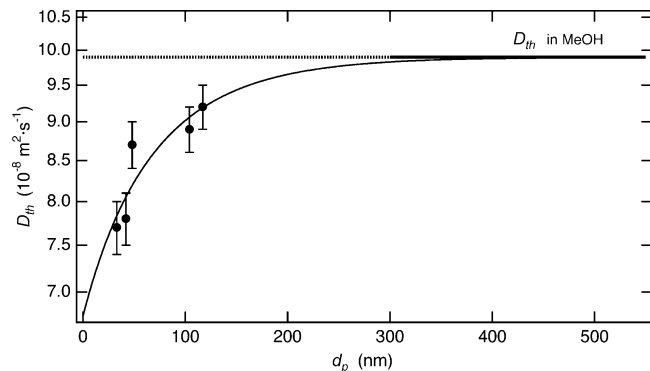


Figure 10. Penetration depth dependence of the apparent thermal diffusivity for the system R6G in MeOH in contact with DEC. The solid line is the best fit of an exponential function.

TABLE 3: Value of the Thermal Diffusivity, D_{th} , Obtained from the Decay of the Diffracted Intensity Measured with Different Transient Evanescence Grating Geometries as a Function of the Penetration Depth, d_p , with the System R6G in MeOH in Contact with DEC

| geometry | d_p (nm) | $D_{th} \times 10^8$ ($\text{m}^2 \cdot \text{s}^{-1}$) |
|-----------|------------|---|
| boxcars | bulk MeOH | 9.9 |
| TIR-probe | 117 | 9.2 |
| TIR-probe | 104 | 8.9 |
| TIR-pump | 48 | 8.7 |
| TIR-pump | 42 | 7.8 |
| all-TIR | 33 | 7.7 |

reproduced with an exponential function rising toward the bulk value of D_{th} at large depth. Interestingly, the value measured at the smallest depth is essentially the same as that in bulk DEC, $D_{th} = 7.4 \times 10^{-8} \text{ m}^2 \text{ s}^{-1}$.⁴⁵

An even stronger difference between interfacial and bulk measurements has been observed with an aqueous solution of R6G in contact with DOD. A D_{th} value of $8 \times 10^{-8} \text{ m}^2 \text{ s}^{-1}$ was measured at $d_p = 72 \text{ nm}$, while the experimental diffusivity constant in bulk water solution amounts to $14.6 \times 10^{-8} \text{ m}^2 \text{ s}^{-1}$. Here again, the D_{th} value measured at the interface is essentially identical with that of pure DOD, $D_{th} \approx 8 \times 10^{-8} \text{ m}^2 \text{ s}^{-1}$.⁴⁶

This result is surprising and differs from the observation reported by Terazima and co-workers that the thermal diffusivity measured at the air/2-propanol and air/1-hexanol interfaces was essentially the same as that in the bulk phases.⁴⁷ Moreover, the fit of an exponential function to the measured data has no physical basis. Indeed in solids, thermal diffusivity depth profiles have been shown to depart strongly from exponentiality.⁴⁸

We explain the penetration depth dependence of D_{th} observed here by the formation of a density phase grating in the transparent apolar phase, DEC or DOD, induced by thermal diffusion from the polar absorbing phase.

The evanescent grating generated in the TIR-pump geometry is a very thin grating, d_p being 50 nm, while Λ is larger by several orders of magnitude, typically around 10 μm . To discuss how such a thin density phase grating can be affected by thermal diffusion, three different directions have to be considered (see Figure 1): (a) the x -axis direction, i.e., the direction along the grating vector, (b) the $+z$ direction perpendicular to the interface toward the polar absorbing phase, and (c) the $-z$ direction, toward the apolar transparent phase. Thermal diffusion along x leads to a washing out of the fringes and thus to a decay of the diffracted intensity as in the case of a thick grating. With 10 μm fringes, this process takes place in the submillisecond time scale. Thermal diffusion along the $\pm z$ -axis leads to an increase of the grating thickness, d . For a thin grating with $d = 50 \text{ nm}$,

TABLE 4: Value of the Amplitude Factor, C^{TE}/Q , for Various Solvents^a

| | solvent | | | |
|--|---------|------------------|------|------|
| | MeOH | H ₂ O | DEC | DOD |
| $C^{TE}/Q \times 10^{10} (\text{m}^3 \cdot \text{J}^{-1})$ | 2.05 | 0.21 | 6.20 | 2.55 |

^a Calculated using data taken from ref 49.

a 2-fold increase of the thickness occurs in the nanosecond time scale. In principle, diffusion along the $+z$ direction should not affect the diffracted intensity, as the decrease of the modulation amplitude of the refractive index, Δn_d^{TE} , is compensated by the larger grating thickness, i.e., a longer interaction length with the probe field (see eq 4). In the TIR-probe geometry, the density grating is thick, and therefore thermal diffusion along $+z$ is irrelevant.

The importance of thermal diffusion in the $-z$ direction depends on the material in contact with the absorbing phase. As the thermal conductivity of air is small ($\lambda_{th} = 2.6 \times 10^{-2} \text{ W m}^{-1} \text{ K}^{-1}$),²⁸ thermal diffusion in the $-z$ direction should not affect significantly the decay of the diffracted intensity at an air/liquid interface, in agreement with the experiment.⁴⁷ On the other hand, Terazima and co-workers have observed a strong acceleration of the decay of the thermal phase grating in a liquid in contact with sapphire,²⁰ the thermal conductivity of the latter being about 3 orders of magnitude larger than that of air.

In the case of the liquid/liquid interface studied here, the thermal conductivity of the transparent apolar phase is only 3 to 4 times smaller than that of the absorbing polar phase and thus heat transfer across the interface must take place. Therefore, a few nanoseconds after grating generation in the absorbing phase, a thin phase grating, with the same fringe spacing as the evanescent grating, is formed by thermal diffusion in the apolar phase. Consequently, the probe beam interacts with this grating as well and the resulting diffracted field adds coherently to that diffracted by the evanescent grating.

Apart from the amount of heat deposited, the modulation amplitude of this new phase grating depends on the various material parameters shown in eq 9. The magnitude of C^{TE}/Q has been calculated with literature values for four solvents and is listed in Table 4.⁴⁹ This table shows that for the same amount of heat deposited, the modulation amplitude Δn_d^{TE} in the apolar phase is substantially larger than that in the polar phase. This larger C^{TE}/Q value in the apolar phase should compensate for its smaller thermal conductivity.

As the thermal diffusivity constant of the polar phase, $D_{th}(p)$, is larger than that of the apolar phase, $D_{th}(a)$, the lifetime of the thermal phase grating in the former phase is smaller than that in the latter medium. If both gratings contribute equally to the diffracted intensity, the intensity decay due to thermal diffusion should be a triexponential function with the time constants $\tau_1 = [(D_{th}(p) + D_{th}(a))q_g^2]^{-1}$, $\tau_2 = [2D_{th}(p)q_g^2]^{-1}$, and $\tau_3 = [2D_{th}(a)q_g^2]^{-1}$ and the relative amplitudes $A_1 = 2A_2 = 2A_3$.

In the case of DEC/MeOH, the simulated decay can be well reproduced with a single-exponential function with $\tau \approx \tau_1$. Therefore, the single-exponential decay of the diffracted intensity observed near the interface should not be surprising.

The penetration depth dependence of D_{th} reported in Figure 10 is related to the different geometries used for the measurements. In the TIR-pump geometry, a thin evanescent grating is first generated in the polar phase. The larger the penetration depth, the larger the amount of heat deposited in the polar phase and the weaker is the relative contribution of the grating formed by thermal diffusion in the apolar phase. In the TIR-probe

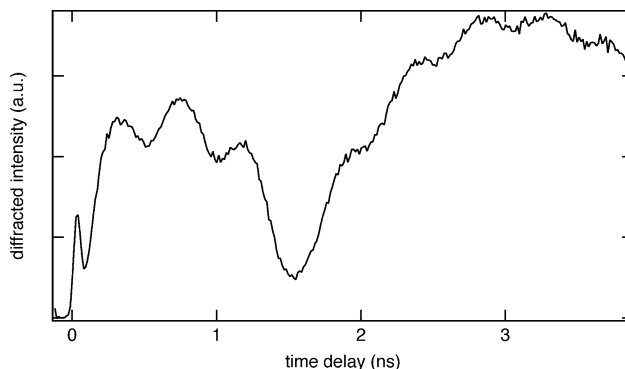


Figure 11. Time profile of the diffracted intensity measured with a 0.2 M solution of R6G in MeOH in contact with DEC using the pump-probe setup and the TIR-probe geometry.

geometry, the effect is even stronger because the grating formed in the polar phase is a thick grating. Finally in the all-TIR geometry, thermal diffusion in the $\pm z$ direction decreases the amplitude of the grating in the polar phase seen by the evanescent probe field. On the other hand, diffusion along the $-z$ direction increases the amplitude and the thickness of the grating in the apolar phase. In this geometry, one monitors essentially the thermal grating in the apolar phase.

Because of the heat transfer between the two phases, it is not possible to determine thermal diffusivity near the interface. This is due to the fact that the thickness of the region of interest is much smaller than the fringe spacing. The smallest fringe spacing can be obtained with counter-propagating pump pulses.⁵⁰ With 532 nm pump pulses, Λ is still larger than 150 nm, i.e., larger than the evanescent grating thickness.

Propagation of Acoustic Wave Packets. Figure 11 shows the time profile of the diffracted intensity measured with the pump-probe technique (TIR-probe geometry) with a high R6G concentration in MeOH in contact with DEC and a high pump intensity. The crossing angle was relatively small and therefore the time-window of the experiment corresponds approximately to a single acoustic period. The two broad humps centered at about 0.7 and 3 ns are thus due to the acoustic modulation of the TG intensity originating from the ES and TE mechanisms. Additionally, a clear oscillation with a period of about 450 ps is visible. The period of this fast oscillating component that vanishes at lower pump intensity is independent of the crossing angle of the pump pulses. This suggests that it is due to a process occurring along the direction normal to the interfacial plane. Indeed, thermal expansion in the illuminated fringes occurs in all three spatial dimensions. Thermal expansion along the grating vector gives rise to acoustic waves of well-defined frequency, while thermal expansion in the $\pm z$ directions generates two acoustic wave packets. The width of these acoustic pulses depends on the thickness of the region where heat has been deposited. Given the high R6G concentration used for this measurement, 90% of the pump energy is absorbed within the first 500 nm of the polar phase. Therefore the acoustic pulses should leave the excitation region within about 500 ps. One pulse propagates in the $+z$ direction, i.e., in the polar phase, while the other, travelling along the $-z$ direction, is partially reflected back at the liquid/liquid interface. The reflection coefficient, r , of an interface for an acoustic pulse propagating from medium 1 to medium 2 is given by

$$r = \frac{w_2 - w_1}{w_2 + w_1} \quad (15)$$

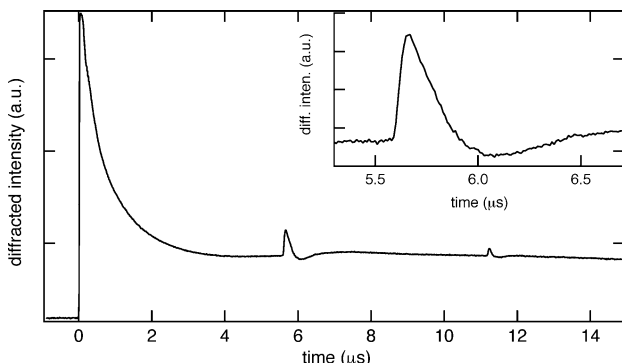


Figure 12. Time profile of the diffracted intensity measured with R6G in MeOH in contact with DEC using the cw-probe setup and the TIR-pump geometry (see text for details).

where w_i is the acoustic impedance of the medium i , $w = \rho v_{ac}$. For the MeOH/DEC interface, r amounts to 0.17. We suggest that this partial reflection leads to a displacement of the interface in the $-z$ direction and that a restoring force, associated with the interfacial tension, sets up an oscillatory motion. This oscillation, which is rapidly damped, perturbs the region probed by the evanescent pulse and leads thus to a periodic modulation of the diffracted intensity. The propagation of an acoustic wave packet generated by photoinduced thermal expansion in a thin solid layer in contact with another solid or a liquid is well documented.^{51–54} However, to our knowledge, such an oscillation observed at a liquid/liquid interface has not been reported so far. This might be due to several factors, such as the use of an evanescent probe beam, the high pump intensity, and also the smaller stiffness of the liquid/liquid interface compared to that of solid/solid and solid/liquid interfaces. However, additional measurements are needed for confirming this hypothesis.

The reflection coefficient of the MeOH/air interface is close to -1 and thus the acoustic wave packet that propagates in the z direction through the polar phase should in principle be nearly totally back reflected. The arrival of this pulse back to the interfacial region, the acoustic echo, should result to a perturbation of the grating and thus to a transient change of the diffracted intensity.^{53,54} Given the thickness of the polar absorbing phase ($d_a > 1$ mm), the roundtrip time of the acoustic wave packet, given by $\tau_r = 2d_a/v_{ac}$, should be of the order of several microseconds. Figure 12 shows the time profile of the diffracted intensity in the microsecond time scale measured with the system R6G in MeOH in contact with DEC using the TIR-pump geometry ($d_p = 42$ nm). Small replica of the initial peak can clearly be observed 5.6 and 11.2 μ s after excitation. The time delays at which these replica appear depend on thickness of the absorbing phase as $t = n2d_a/v_{ac}$ ($n = 1, 2$), as expected for the acoustic echoes. With absorbing layers thinner than 3 mm, up to three echoes can be observed. Moreover, the number and intensity of the echoes increases with increasing R6G concentration. This can be explained by the larger amount of heat deposited by the evanescent pump pulses at high dye concentration.

These echoes could only be observed when using the photomultiplier tube in the saturation regime. Indeed, the duration of the acoustic pulse should be of the order of $2d_p/v_{ac}$, i.e., less than about 100 ps. Such a short pulse can clearly not be detected in a time-window of several microseconds. However, using the photodetector in the saturation regime leads to a strongly distorted response and, because of this, the acoustic echoes can be observed. This saturation is responsible for the absence of oscillations due to the acoustic waves that can be seen in Figure 7. Knowledge of the arrival time of the echo

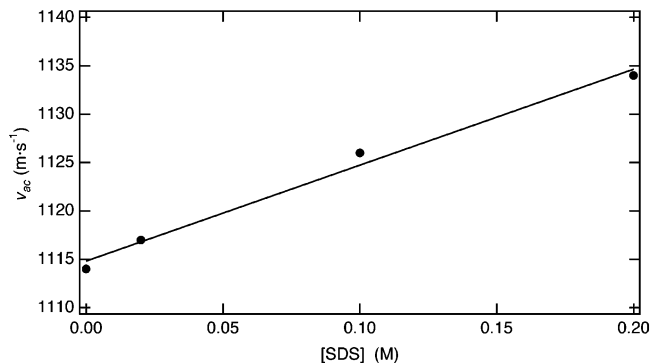


Figure 13. Speed of sound measured in a solution of MG in MeOH with various concentrations of SDS and best linear fit.

TABLE 5: Speed of Sound, v_{ac} , Measured in Bulk MeOH and in MeOH in Contact with DEC with Different SDS Concentrations and at Various Times, t , after Sample Preparation, and Effective SDS Concentration in MeOH Near the Interface, $[SDS]_{int}$

| t (h) | $[SDS]_{bulk}$ (M) | v_{ac} (m·s ⁻¹) | | |
|---------|--------------------|-------------------------------|-----------|-------------------|
| | | bulk | interface | $[SDS]_{int}$ (M) |
| 1 | 0.02 | 1117 | 1129 | 0.14 |
| 24 | 0.02 | | 1135 | 0.20 |
| 1 | 0.1 | 1126 | 1137 | 0.22 |
| 24 | 0.1 | | 1143 | 0.28 |
| 1 | 0.2 | 1134 | 1147 | 0.32 |
| 24 | 0.2 | | 1159 | 0.44 |

would in principle allow the precise measurement of its profile without this distortion problem. However, this goes beyond the scope of this paper.

Effect of a Surfactant. As natural membranes are constituted of lipid bilayers, the addition of an alkyl surfactant to the liquid/liquid system results in a more realistic model of a biological interface.⁵⁵ Amphiphilic molecules are known to adsorb at interfaces, and this process should thus be observable with the TEG technique. To test this with the system SDS in DEC/MeOH, some experiments have first been performed in bulk MeOH. As shown in Figure 13, the speed of sound measured in a bulk solution of MG in MeOH increases upon addition of SDS. The experimental geometry was the same for all measurements, and only the sample was changed. Therefore, the relative error between the v_{ac} values is considerably smaller than that in Figure 9. The measured speed of sound does not depend on the age of the sample. The same value was obtained 3 or 22 h after SDS addition, confirming that the composition of sample is stable and free from micellization. From this figure, a direct relationship between the speed of sound and the SDS concentration in MeOH can be obtained:

$$v_{ac} = 1115 \text{ ms}^{-1} + 99[\text{SDS}] \text{ ms}^{-1} \text{ M}^{-1} \quad (16)$$

On the other hand, addition of SDS has no significant effect on the thermal diffusivity.

In a second stage, solutions of R6G in MeOH with various SDS concentrations were poured on DEC in the sample cell for measurements at interfaces. The speed of sound was then measured using the cw-probe setup 1 and 24 h after the sample preparation. As shown in Table 5, the speed of sound measured near the interface is substantially larger than that in the bulk at the same SDS concentration. Moreover, the speed of sound depends on the age of the sample, the value measured 1 day after sample preparation being clearly larger than that recorded after 1 h. This larger v_{ac} value is ascribed to the adsorption of the surfactant molecules at the interface. This results in a local

increase of SDS concentration and hence in a larger speed of sound. The effective SDS concentrations in the volume probed by the evanescent TG measurements calculated using eq 16 are listed in Table 5. In principle, the adsorption at the interface is a fast process (10^{-3} –10 s),^{56,57} and therefore the difference of the speed of sound measured after 1 h and 1 day might not be related only to an accumulation of SDS near the interface but also to a specific arrangement of the SDS molecules, such as the formation of a multilayer. A better insight into the adsorption mechanism of SDS at this interface would require measurement of the interfacial pressure.^{58,59}

Interestingly, the relative magnitude of the two mechanisms responsible for the generation of acoustic waves, i.e., thermal expansion and electrostriction, changes as a function of time. One hour after the sample preparation with 0.2 M SDS, the TE:ES ratio is 1.7:1, while it increases to 2.5:1 and 4.2:1 after 2 and 24 h, respectively. This effect can have two origins: (1) an accumulation of R6G near the interfacial region induced by the presence of SDS, and (2) a variation of the thermoelastic properties of the R6G solution upon addition of SDS.

Finally, as in the bulk measurements, the thermal diffusivity, D_{th} , is independent of SDS concentration.

Conclusion

This study shows that the transient evanescent grating techniques can be considered as additional tools for investigating liquid/liquid interfaces. Depending on the geometry used, a penetration depth as small as 40 nm can be achieved. In principle, this selectivity can be further improved by working at shorter wavelengths. In this investigation, we have only looked at the time evolution of density phase gratings, which allows the determination of thermoacoustic properties of the sample. In such measurements, the “inert” transparent phase plays a very important role. First, it actively contributes to the transient grating signal through its nonresonance response. When properly taken into account, this effect can be used deliberately for internal calibration. Second, it acts as a thermal conductor and thus inhibits the determination of the thermal diffusivity in the absorbing phase near the interface. The results show that the sound velocity in the polar phase in contact with an apolar liquid is essentially the same as that in the bulk. This is not really surprising as the layer probed by the transient evanescent grating techniques is still much thicker than the interfacial layer. It is, however, possible to monitor the accumulation of a surfactant near the interface.

Additionally, we have demonstrated that acoustic echoes can be measured at liquid/liquid interfaces, and used to determine the thickness of liquid layers. This technique is already common in solid-state microengineering, but inducing ultrasonics at the interface between two immiscible liquids is in principle more difficult. The methods used here can overcome this problem, thus opening new possibilities with unconventional systems.

Finally, these techniques are of course not limited to the investigation of thermoacoustic properties. As they are sensitive to absorbance changes as well, population and molecular reorientation dynamics near liquid/liquid interfaces can also be investigated. Such studies will be reported in the near future.

Acknowledgment. This work was supported by the Fonds National Suisse de la Recherche Scientifique through project No. 200020-100014.

References and Notes

- Volkov, A. G. E. *Liquid interfaces in chemical, biological, and pharmaceutical applications*; Marcel Dekker: New York, 2001.
- Shen, Y. R. *The Principles of Nonlinear Spectroscopy*; J. Wiley: New York, 2003.
- Richmond, G. L. *Chem. Rev.* **2002**, *102*, 2693.
- Eisenthal, K. B. *Chem. Rev.* **1996**, *96*, 1343.
- Brevet, P.-F. *Surface Second Harmonic Generation*; Presses polytechniques et universitaires romandes: Lausanne, Switzerland, 1997.
- Fishman, I. M.; Marshall, C. D.; Tokmakoff, A.; Fayer, M. D. *J. Opt. Soc. Am. B* **1993**, *10*, 1006.
- Ikeda, S.; Katayama, K.; Tanaka, T.; Sawada, T.; Tsuyumoto, I.; Harata, A. *J. Chem. Phys.* **1999**, *111*, 9393.
- De Serio, M.; Bader, A. N.; Heule, M.; Zenobi, R.; Deckert, V. *Chem. Phys. Lett.* **2003**, *380*, 47.
- Rumbles, G.; Bloor, D.; Brown, A. J.; DeMello, A. J.; Crystall, B.; Phillips, D.; Smith, T. A. In *Microchemistry, spectroscopy and chemistry in small domains*; Masuhara, H., DeSchryver, F. C., Kitamura, N., Tamai, N., Eds.; Elsevier Science: Amsterdam, The Netherlands, 1994; p 269.
- Ishizaka, S.; Kitamura, N. *Bull. Chem. Soc. Jpn.* **2001**, *74*, 1983.
- Tsukahara, S.; Watarai, H. *Chem. Lett.* **1999**, *89*.
- Fayer, M. D. *Annu. Rev. Phys. Chem.* **1982**, *33*, 63.
- Eichler, H. J.; Günter, P.; Pohl, D. W. *Laser-Induced Dynamic Gratings*; Springer-Verlag: Berlin, Germany, 1986.
- Fourkas, J. T.; Fayer, M. D. *Acc. Chem. Res.* **1992**, *25*, 227.
- Högemann, C.; Pauchard, M.; Vauthay, E. *Rev. Sci. Instrum.* **1996**, *67*, 3449.
- Terazima, M. *Adv. Photochem.* **1998**, *24*, 255.
- Miller, R. J. D.; Casalegno, R.; Nelson, K. A.; Fayer, M. D. *Chem. Phys.* **1982**, *72*, 371.
- Sainov, V. O. *J. Chem. Phys.* **1996**, *104*, 6901.
- Tamai, N.; Asahi, T.; Ito, T. In *Microchemistry, spectroscopy and chemistry in small domains*; Masuhara, H., DeSchryver, F. C., Kitamura, N., Tamai, N., Eds.; Elsevier Science: Amsterdam, The Netherlands, 1994; p 241.
- Terazima, M.; Kojima, Y.; Hirota, N. *Chem. Phys. Lett.* **1996**, *259*, 451.
- Brodard, P.; Vauthay, E. *Rev. Sci. Instrum.* **2003**, *74*, 725.
- Nelson, K. A.; Casalegno, R.; Miller, R. J. D.; Fayer, M. D. *J. Chem. Phys.* **1982**, *77*, 1144.
- Vauthay, E.; Henseler, A. *J. Phys. Chem.* **1995**, *99*, 8652.
- Brodard, P.; Vauthay, E. *Chem. Phys. Lett.* **1999**, *309*, 198.
- Henseler, A.; Vauthay, E. *J. Photochem. Photobiol. A* **1995**, *91*, 7.
- Ippen, E. P.; Shank, C. V.; Bergman, A. *Chem. Phys. Lett.* **1976**, *38*, 611.
- Vauthay, E.; Suppan, P. *Chem. Phys.* **1989**, *139*, 381.
- Handbook of Chemistry and Physics*; Lide, D. R., Ed.; CRC Press: Boca Raton, FL, 2001; Vol. 82n.
- Schaaffs, W. Z. *Phys. Chem.* **1944**, *194*, 28.
- Oswal, S. L.; Patel, N. B. *J. Chem. Eng. Data* **2000**, *45*, 225.
- Bialkowski, S. E. *Photothermal spectroscopy methods for chemical analysis*; Wiley: New York, 1996.
- Balderas-Lopez, J. A.; Mandelis, A.; Garcia, J. A. *Anal. Sci.* **2001**, *17*, s519.
- Ohmori, T.; Kimura, Y.; Hirota, N.; Terazima, M. *Phys. Chem. Chem. Phys.* **2001**, *3*, 3994.
- Hess, P. *Phys. Today* **2002**, *42*.
- Glorieux, C.; Van de Rostyne, K.; Beers, J. D.; Gao, W.; Petillion, S.; Van Riet, N.; Nelson, K. A.; Allard, J. F.; Gusev, V. E.; Lauriks, W.; Thoen, J. *Rev. Sci. Instrum.* **2003**, *74*, 465.
- Kasinski, J. J.; Gomez-Jahn, L. A.; Faran, K. J.; Gracewski, S. M.; Miller, R. J. D. *J. Chem. Phys.* **1989**, *90*, 1253.
- Gracewski, S. M.; Miller, R. J. D. *J. Chem. Phys.* **1995**, *103*, 1191.
- Zhang, Z.; Tsuyumoto, I.; Takahashi, S.; Kitamori, T.; Sawada, T. *J. Phys. Chem. A* **1997**, *101*, 4163.
- Daikhin, L. I.; Kornyshev, A. A.; Urbakh, M. *Chem. Phys. Lett.* **1999**, *309*, 137.
- Trojanek, A.; Krtil, P.; Samec, Z. *Electrochem. Commun.* **2001**, *3*, 613.
- Jeng, U. S.; Esibov, L.; Crow, L.; Steyerl, A. *J. Phys. Condens. Matter* **1998**, *10*, 4955.
- Penzkofer, A.; Lu, Y. *Chem. Phys.* **1986**, *103*, 399.
- Gumy, J.-C.; Vauthay, E. *J. Phys. Chem.* **1996**, *100*, 8628.
- Fischer, M.; Georges, J. *Chem. Phys. Lett.* **1996**, *260*, 115.
- Wu, G.; Fiebig, M.; Leipertz, A. *Int. J. Heat Mass Transfer* **1988**, *31*, 1471.
- Watanabe, H.; Song, D. J. *Int. J. Thermophys.* **2001**, *23*, 337.
- Yasumoto, K.; Hirota, N.; Terazima, M. *Phys. Rev. B* **1999**, *60*, 9100.
- Nicolaides, L.; Mandelis, A.; Beingessner, C. *J. Appl. Phys.* **2001**, *89*, 7879.

(49) Riddick, J. A.; Bunger, W. B. *Organic Solvents*; J. Wiley: New York, 1970.

(50) Genberg, L.; Bao, Q.; Gracewski, S.; Miller, R. J. D. *Chem. Phys.* **1989**, *131*, 81.

(51) Thomsen, C.; Strait, J.; Vardeny, Z.; Maris, H. J.; Tauc, J.; Hauser, J. *J. Phys. Rev. Lett.* **1984**, *53*, 989.

(52) Thomsen, C.; Grahn, H. T.; Maris, H. J.; Tauc, J. *J. Phys. Rev. B* **1986**, *34*, 4129.

(53) Crimmins, T. F.; Maznev, A. A.; Nelson, K. A. *Appl. Phys. Lett.* **1999**, *74*, 1344.

(54) Slayton, R. M.; Nelson, K. A. *J. Chem. Phys.* **2004**, *120*, 3908.

(55) Cavic, B. A.; Chu, F. L.; Furtado, L. M.; Ghafouri, S.; Hayward, G. L.; Mack, D. P.; McGovern, M. E.; Su, H.; Thompson, M. *Faraday Discuss.* **1997**, *107*, 159.

(56) Haslam, S.; Croucher, S. G.; Hickman, C. G.; Frey, J. G. *Phys. Chem. Chem. Phys.* **2000**, *2*, 3235.

(57) Takahashi, T.; Yui, H.; Sawada, T. *J. Phys. Chem. B* **2002**, *106*, 2314.

(58) Watry, M. R.; Richmond, G. L. *J. Am. Chem. Soc.* **2000**, *122*, 875.

(59) Hari, K.; Seo, Y.-S.; Satija, S. *J. Phys. Chem. B* **2004**, *108*, 11442.